

# Resolving diffusion signatures in distant pulsar halos with current and future experiments

Yong-Jian Wei<sup>a,b,\*</sup>, En-Sheng Chen<sup>a,c,†</sup>, Kun Fang<sup>a,‡</sup> and Xiao-Jun Bi<sup>a,b,c,§</sup>

<sup>a</sup>*Key Laboratory of Particle Astrophysics, Institute of High Energy Physics,  
Chinese Academy of Sciences, Beijing 100049, China*

<sup>b</sup>*University of Chinese Academy of Sciences, Beijing 100049, China*

<sup>c</sup>*TIANFU Cosmic Ray Research Center, Chengdu, Sichuan, China*

(Dated: March 6, 2026)

## Abstract

$\gamma$ -ray pulsar halos are produced by electron-positron pairs that diffuse away from the pulsar and scatter off background photons. Their morphology serves as an ideal probe for studying cosmic-ray propagation on scales of several tens of parsecs. However, the number of firmly identified pulsar halos remains limited, primarily because current  $\gamma$ -ray experiments, limited by angular resolution, struggle to resolve the diffusion signatures of distant candidates ( $> 1$  kpc). In this work, we investigate the prospects for identifying pulsar halo candidates through morphological discrimination using simulations of two advanced  $\gamma$ -ray experiments: the Kilometer Square Array of the Large High Altitude Air Shower Observatory (LHAASO-KM2A) and the Cherenkov Telescope Array (CTA, under construction). Using mock observations with realistic instrumental responses, we quantitatively assess the ability of each experiment to distinguish diffusion-based halo morphologies from alternative spatial models. Our analysis indicates that if LHAASO-KM2A could improve its angular resolution by 40%, it would be capable of resolving several prominent pulsar-halo candidates, namely the halos around pulsars J1831-0952, J0248+6021, and J0359+5414. CTA holds an advantage in resolving the morphology of sources beyond  $\approx 1.5$  kpc owing to its superb angular resolution. By extending exposure times to hundreds of hours, CTA is expected to achieve morphological identification for all known pulsar-halo candidates.

---

\* weiyongjian@ihep.ac.cn

† chenes@ihep.ac.cn

‡ fangkun@ihep.ac.cn

§ bixj@ihep.ac.cn

## I. INTRODUCTION

In 2007, the water Cherenkov experiment Milagro discovered  $\gamma$ -ray emission extending  $\approx 3^\circ$  around the bright  $\gamma$ -ray pulsar Geminga [1]. This large extended halo was difficult to interpret by the pulsar itself or its associated bow-shock pulsar wind nebula [2, 3]. A decade later, the High-Altitude Water Cherenkov Observatory (HAWC) observed this halo with improved angular resolution and sensitivity, revealing that a diffusion model of electrons could perfectly explain its spatial distribution [4]. This finding pointed to the most likely origin of the Geminga halo: electron-positron pairs ( $e^\pm$ ) born in the pulsar escape into the interstellar medium (ISM) and, as they diffuse in the turbulent magnetic field, produce extended  $\gamma$ -ray emission through inverse Compton scattering with background photons. Consequently, a new class of astrophysical sources emerged, named pulsar halos or TeV halos. The morphology of a pulsar halo is a clear projection of the spatial distribution of its parent  $e^\pm$ , making it a unique probe for studying the cosmic-ray propagation in a specific ISM region [5–8].

Based on surveys of TeV  $\gamma$ -ray sources conducted by wide-field experiments HAWC and the Large High Altitude Air Shower Observatory (LHAASO), the number of confirmed or candidate pulsar halos has reached around ten [9, 10]. However, apart from the Geminga halo and the Monogem halo [4], the corresponding pulsars for other potential halos are all located at distances exceeding 1 kpc, resulting in significantly smaller angular extensions of these halos. In the case of LHAASO J0621+3755, the morphology measurements, affected by instrumental angular resolution, cannot distinguish between a diffusion model and mathematical templates such as disk or Gaussian profiles [11]. The lack of clear diffusion signatures in the observed morphology complicates the confirmation of pulsar halos.

To reliably expand the sample size of pulsar halos, enhanced instrumental angular resolution plays a crucial role. The Cherenkov Telescope Array (CTA, [12]), currently under construction, will achieve unprecedented angular resolution ( $< 0.05^\circ$  above 10 TeV [13]) in  $\gamma$ -ray astronomy, along with significantly improved sensitivity compared to current atmospheric Cherenkov experiments. This will serve as the primary means of identifying diffusion signatures in distant pulsar halos. On the other hand, LHAASO, with its wide field of view and long exposure time, remains indispensable for precise observations of relatively nearby pulsar halos. In the future, LHAASO plans to integrate deep learning techniques to im-

prove directional reconstruction, thereby achieving better angular resolution for resolving the morphologies of more distant pulsar halos. Based on these prospects, this study examines the potential of experiments to decipher diffusion signatures in candidate pulsar halos and evaluates how enhancements in angular resolution or exposure time can boost the identification.

The paper is organized as follows. Section II presents a simplified template of pulsar halos that effectively captures their morphological characteristics. Section III introduces the  $\gamma$ -ray experiments and the methods for simulating pulsar halo signals based on experimental information. Section IV presents the statistical approach used for morphological discrimination. Section V demonstrates the capability of experiments to conduct morphological tests on pulsar halos. Section VI is the conclusion.

## II. DIFFUSION-BASED PULSAR HALO MODEL

Electron-positron pairs produced by pulsars can be accelerated to energies as high as 100 TeV by relativistic shocks in PWNe, after which they continuously escape into the ISM. When a PWN evolves into the bow-shock stage, its size remains on the order of  $\sim 1$  pc for an extended period under the confinement of the ISM ram pressure [14], which is much smaller than the characteristic diffusion scale of the escaped  $e^\pm$ . Consequently, the propagation of the parent  $e^\pm$  in pulsar halos can be regarded as a diffusion–radiation-loss problem under the point-source assumption. Under this scenario, the  $\gamma$ -ray surface brightness of a pulsar halo can be approximately described by the following parameterization [4]:

$$f(\theta, E_\gamma) = f_0 \left( \frac{E_\gamma}{30 \text{ TeV}} \right)^{-\alpha} e^{-E_\gamma/E_c} \times \frac{1.22}{\pi^{3/2}\theta_d(\theta + 0.06\theta_d)} e^{-(\theta/\theta_d)^2}, \quad (1)$$

where  $f_0$  is the normalization at 30 TeV,  $\alpha$  is the spectral index,  $E_c$  is the cutoff energy,  $\theta$  is the angular distance from the pulsar, and  $\theta_d$  is the characteristic angular extension of the halo, which can be dependent on  $E_\gamma$ . The  $\gamma$ -ray spectrum is assumed to be a power-law with an exponential cutoff (ECPL) form, effectively reflecting that the parent  $e^\pm$  originate from a shock-acceleration process.

The spatial distribution term in Eq. (1) exhibits a pronounced centrally-peaked profile, which differs significantly from the uniform disk template commonly used to describe the profile of supernova remnants. Additionally, a Gaussian template is also generally used

in  $\gamma$ -ray astronomy to characterize the morphology of extended sources with a centrally-peaked profile. Yet, it too remarkably differs from Eq. (1): within the range  $0.06\theta < \theta < \theta_d$ , Eq. (1) decreases sharply with increasing  $\theta$ , exhibiting a steeper decline than the Gaussian distribution. However, all these distinctions may become blurred due to the insufficient instrumental angular resolution or the limited photon statistics.

In this work, we aim to investigate the capability of  $\gamma$ -ray experiments to identify pulsar halos through morphological discrimination. We adopt the diffusion-based parameterization (hereafter referred to as diffusion model) presented by Eq. (1) to describe the morphology of pulsar halos, and consider the disk and Gaussian models as representative alternatives for non-halo origins.

The variables that primarily reflect differences among pulsar halos are the pulsar distance  $d$  and its spin-down luminosity  $\dot{E}$ . Generally, morphology discrimination becomes more difficult for more distant sources or those with lower spin-down luminosity. At present, the  $\gamma$ -ray energy spectrum and morphology of the Geminga halo have the most precise measurements. For simplicity, we assume that all the halos share the same spectral shape as the Geminga halo, where the  $\gamma$ -ray energy spectrum of the Geminga halo is obtained by fitting the HAWC data [15], which yields  $\alpha = 1.49$  and  $E_c = 22.7$  TeV.

Additionally, we assume that the  $f_0$  and  $\theta_d$  of a pulsar halo scale depending on the ratio of its pulsar distance to that of Geminga:  $f_0 = f_{0,G}(d/d_G)^{-2}$ ,  $\theta_d = \theta_{d,G}(d/d_G)^{-1}$ , where  $\theta_{d,G}$  is set to  $5.5^\circ$  as measured by HAWC [4]. For simplicity,  $\theta_d$  is assumed to be energy independent.

### III. INSTRUMENTAL SETUP AND MONTE CARLO DATA

Ground-based observations of high-energy  $\gamma$  rays are performed indirectly by measuring secondary particles generated in extensive air showers initiated by primary gamma rays. Two main experimental techniques are employed to detect such emission. The first is the Imaging Atmospheric Cherenkov Telescope (IACT) technique, which observes Cherenkov light flashes generated by relativistic shower particles propagating through the atmosphere during clear, moonless nights. The second is the extensive air shower (EAS) technique, which detects secondary shower particles directly at ground level. In this work, we focus on two representative instruments employing these approaches: CTA and the Kilometer Square

Array of LHAASO (LHAASO-KM2A).

### A. CTA

CTA will be the flagship next-generation instrument in  $\gamma$ -ray astronomy, covering photon energies from 20 GeV to 300 TeV. It is designed to achieve an energy resolution better than 10% and a substantially improved angular resolution compared to existing  $\gamma$ -ray telescopes. CTA will operate as a global observatory with two sites: a Northern Hemisphere array (CTA-North) located on La Palma, Spain, and a Southern Hemisphere array (CTA-South) located at Paranal, Chile. In the so-called Alpha Configuration, CTA-North will consist of four Large-Sized Telescopes (LSTs) and nine Medium-Sized Telescopes (MSTs), while CTA-South will comprise 14 MSTs and 37 Small-Sized Telescopes (SSTs). The primary mirror diameters of the LSTs, MSTs, and SSTs are 23 m, 11.5 m, and 4.3 m, respectively. Their corresponding fields of view are larger than  $4.5^\circ$ ,  $7^\circ$ , and  $8^\circ$  [16].

Instrument Response Functions (IRFs)—including angular and energy resolutions, effective area, and expected background rates—are commonly used to derive differential sensitivities and to enable comparisons between different gamma-ray instruments. To facilitate a direct comparison with LHAASO-KM2A under similar sky coverage, we adopt the CTA-North IRFs for on-axis observations. These IRFs are publicly available through the Zenodo repository [17]. Following standard event selection procedures, including  $\gamma$ -hadron separation cuts, we obtain the photon effective area and residual background rates, consistent with the methodology described in Ref. [18].

### B. LHAASO-KM2A

LHAASO is a new-generation  $\gamma$ -ray and cosmic-ray observatory located at an altitude of 4410 m in Daocheng, Sichuan province, China ( $29^\circ 21' 31''$  N,  $100^\circ 08' 15''$  E) [19]. It consists of three sub-arrays: the LHAASO-KM2A, the Water Cherenkov Detector Array (LHAASO-WCDA), and the Wide Field-of-view Cherenkov Telescope Array (LHAASO-WFCTA). Partial operation of LHAASO began in 2019, and the full construction was completed in 2021. LHAASO-KM2A is composed of 5216 electromagnetic detectors (EDs) and 1188 muon detectors (MDs), covering an area of  $1.3 \text{ km}^2$ . The EDs (MDs) are deployed with spacings of

15 m (30 m). The EDs are plastic scintillation detectors that measure the electromagnetic component of EASs and are designed primarily for event reconstruction. The MDs detect the muonic component of EASs and are mainly used for cosmic-ray background discrimination. High-energy  $\gamma$ -ray events above 10 TeV are predominantly recorded by KM2A. The array has a wide field of view of approximately 2 sr and operates with a nearly full duty cycle, providing unprecedented sensitivity for surveying the  $\gamma$ -ray sky at energies above 20 TeV.

We adopt the LHAASO-KM2A instrument response IRFs calibrated using observations of the Crab Nebula [20]. Specifically, we use the IRFs corresponding to a zenith angle of  $\theta = 20^\circ$ , ensuring consistency with those released by the other experiments considered in this work. The expected background rate is derived by convolving the all-particle cosmic-ray flux [21] with the effective area. This effective area is obtained from the photon effective area by first dividing by the  $\gamma$ -ray selection efficiency and then multiplying by the cosmic-ray rejection power reported in Ref. [20]. Using this procedure, we obtain the angular resolution, effective area, and expected background rate consistent with those reported in Ref. [18].

### C. Monte Carlo data

A direct comparison between the LHAASO-KM2A and CTA performance is now possible, since the same energy binning—namely 0.2 per decade in logarithmic scale—is adopted for both instruments. Based on their respective performance characteristics and the energy range relevant for halo spectral measurements, we consider energies from 10 TeV to 100 TeV for LHAASO-KM2A and from 1 TeV to 100 TeV for CTA.

Owing to its pointing observation mode and imaging camera, CTA achieves an excellent angular resolution. At 30 TeV, the  $1\sigma$  width of the point spread function (PSF) is  $\sigma_{\text{PSF}} \sim 0.03^\circ$  for CTA, compared to  $\sigma_{\text{PSF}} \sim 0.3^\circ$  for LHAASO-KM2A. However, since CTA detects Cherenkov light produced by air showers, it can operate only under clear, dark-sky conditions. In contrast, LHAASO-KM2A has a nearly full duty cycle and can operate continuously, both day and night.

For a given extended halo, the differential flux at any spatial position and energy is determined by the assumed spectral and morphological models. The expected number of signal events,  $N_s$ , per energy bin and per spatial pixel within the region of interest (ROI)

is calculated by folding the model flux with the instrument response functions, including PSF, and multiplying by the effective area, observation time, and solid angle. In the work, model flux is generated by the diffusion morphology and ECPL spectrum introduced in Section 2.1. The number of background events,  $N_b$ , is computed from the background rate, which is assumed to be constant in time. Using a toy Monte Carlo (toyMC) approach, the mock observed event counts,  $N_{\text{on}}$ , are generated by drawing Poisson realizations of  $N_s + N_b$ .

#### IV. MORPHOLOGICAL DISCRIMINATION METHOD

For a given  $d$  and  $\dot{E}$ , mock data can be generated based on the diffusion model through the toyMC technique outlined in Section III C. Next, the simulated data is fitted with the model to be tested using the maximum-likelihood method to determine the best-fit parameters. Subsequently, we evaluate the best-fit model using a specific statistical test to obtain a decision for this single trial.

We repeat the above test multiple times and compile the decision from each trial. The proportion of trials in which the diffusion model is correctly chosen (or the wrong model is rejected) relative to the total number of trials is defined as the power of the test. The power reflects the capability of the considered experiment to discriminate the diffusion model.

##### A. Likelihood function

In the ROI, a joint maximum-likelihood fit is performed over energy and spatial bins. Assuming Poisson statistics, the likelihood function is written as

$$\ln \mathcal{L} = \sum_{i=1}^m \sum_{j=1}^n \ln [P(N_{ij}^{\text{on}} | N_{ij}^{\text{b}} + N_{ij}^{\text{s}})], \quad (2)$$

where  $P$  denotes the Poisson probability distribution,  $i$  labels the  $i$ -th energy bin and  $j$  the  $j$ -th spatial pixel. Here,  $N_{ij}^{\text{on}}$  is the number of observed events, while  $N_{ij}^{\text{b}}$  and  $N_{ij}^{\text{s}}$  are the expected background and signal counts, respectively.

The signal expectation  $N_{ij}^{\text{s}}$  is determined by the spatial model under test (Gaussian, disk, or diffusion) and the ECPL spectral model outlined in Section II, folded with the instrument response functions. The free parameters consist of  $f_0$ ,  $\alpha$ ,  $E_c$ , and the angular width of the spatial model. The maximum likelihood is searched using the MIGRAD algorithm embedded

in the Minuit Minimization package<sup>1</sup>. Larger  $\ln \mathcal{L}$  values indicate a stronger preference for the presence of an extended source with the assumed morphology.

## B. Single trial

We adopt two distinct statistical metrics for a single trial to discriminate among different spatial models: the Akaike Information Criterion (AIC) and the  $\chi^2$  goodness-of-fit test. When data samples are sufficient, discriminating in favor of the diffusion model over a wrong model is generally easier than rejecting the wrong model. Therefore, the AIC typically yields higher statistical power than the  $\chi^2$  test. However, compared to the AIC, the decision criterion of the  $\chi^2$  test can be explicitly linked to a probability, which also provides valuable reference for our study.

1. AIC: Since the diffusion model and the alternative models are non-nested, the likelihood ratio test and Wilks' theorem cannot be directly applied to assess the statistical significance of their differences. Therefore, we employ the AIC as a model selection metric, which is widely used in data analysis for comparing non-nested models. The AIC is defined as

$$\text{AIC} = 2k - 2 \ln \mathcal{L}_{\max}, \quad (3)$$

where  $k$  is the number of free parameters in the model and  $\mathcal{L}_{\max}$  is the maximum likelihood. To compare different spatial hypotheses, we define

$$\Delta\text{AIC} = \text{AIC} - \text{AIC}_{\text{diffusion}}, \quad (4)$$

where  $\text{AIC}_{\text{diffusion}}$  corresponds to the diffusion model. Smaller values of  $\Delta\text{AIC}$  indicate a preference for the alternative model. We adopt  $\Delta\text{AIC} > 6$  as the criterion for model discrimination, which represents strong evidence in favor of the diffusion model.

2.  $\chi^2$  test: The  $\chi^2$  statistic provides a straightforward and intuitive way to assess the compatibility between different spatial hypotheses and the mock data. When alternative spatial models, such as Gaussian or disk profiles, are fitted to the one-dimensional radial brightness profiles generated by the diffusion model, they generally yield poorer

---

<sup>1</sup> [https://root.cern.ch/doc/master/group\\_\\_Minuit01d.html](https://root.cern.ch/doc/master/group__Minuit01d.html)

$\chi^2$  values than the diffusion model, as shown in Fig. 1. As the statistical quality of the data improves, these discrepancies become more pronounced, allowing incorrect models to be excluded based on their diminished goodness of fit. We adopt a  $2\sigma$  exclusion criterion (i.e., p-value  $< 0.05$ ) as the condition for model discrimination. Models that are rejected at or above this significance level are considered distinguishable from the diffusion scenario.

It has been confirmed that the  $\chi^2$  test is applicable since the sample size in each bin is sufficiently large (greater than 10), ensuring that the Poisson fluctuations can be well approximated by Gaussian statistics.

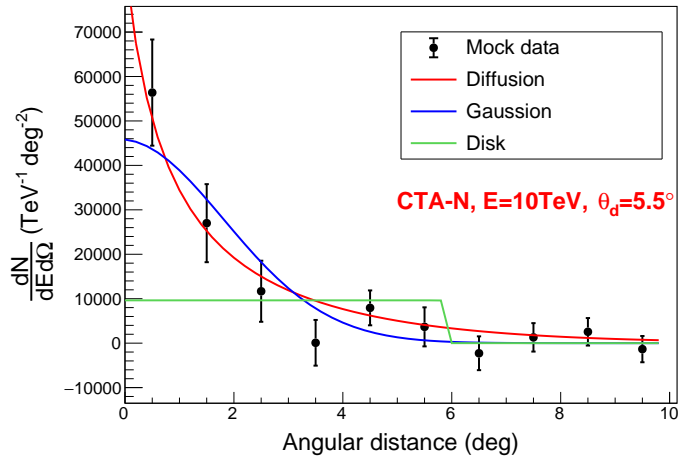


FIG. 1. Radial  $\gamma$ -ray brightness profile of a pulsar halo with the Geminga parameters. The black points represent mock profile data of CTA-North (50 h) generated from the diffusion model. The red, blue, and green curves show the best-fit diffusion, Gaussian, and disk models, respectively.

### C. Statistical power threshold

To mitigate the impact of statistical fluctuations arising from a single Monte Carlo realization, we perform 1000 independent toyMC simulations for each parameter configuration and obtain the corresponding statistical power.

We establish a statistical power threshold of 0.8, meaning that at least 800 out of 1000 realizations must satisfy the discrimination criterion (either the  $\Delta\text{AIC} > 6$  condition or the

$2\sigma$   $\chi^2$  exclusion). When a specific combination of  $d$  and  $\dot{E}$  yields a statistical power of 0.8, it indicates that the diffusion signature of the pulsar halo under these parameters can be resolved by the considered experiment. Consequently, we can determine a critical curve in the  $d - \dot{E}$  plane, above which lies the parameter space where diffusion signatures can be distinguished.

## V. RESULTS

The results of the morphological discrimination analysis are summarized in Fig. 2, i.e., the critical curves in the  $d - \dot{E}$  plane introduced in Section IV C. The four subfigures correspond to different combinations of statistical criteria and competing spatial templates: the AIC and the  $\chi^2$  test, each applied to comparisons between the diffusion-based halo model and Gaussian or disk spatial templates. In each subfigure, four discrimination curves are shown, representing different experimental configurations: LHAASO-KM2A (blue solid line), LHAASO-KM2A with PSF improved by 40% (blue dashed line), CTA-North with 50 h exposure (red solid line), and CTA-North with 200 h exposure (red dashed line).

The positions of confirmed or potential pulsar halos are overlaid for reference, including the Geminga halo and the Monogem halo [4, 15], LHAASO J0621+3755 [22], LHAASO J0249+6022 [23], HESS J1831–098 [24, 25], and the source around PSR J0359+5414 [26]. In addition, we consider pulsar-associated sources from the LHAASO catalog with characteristic ages greater than 20 kyr, excluding younger systems that may still be dominated by emission from initial pulsar wind nebulae. Halo candidates located outside the LHAASO field of view are not shown [27, 28].

A general trend is that the AIC-based method yields less restrictive discrimination conditions than the  $\chi^2$  test. For the same spatial template and instrumental configuration, the AIC criterion identifies a larger region of the  $d - \dot{E}$  parameter space as distinguishable, allowing more halo candidates to be resolved by both CTA and LHAASO-KM2A. This behavior is expected, since the AIC is designed for relative model comparison between non-nested hypotheses by explicitly accounting for differences in model complexity, whereas the  $\chi^2$  test primarily evaluates the absolute goodness of fit of a given model based on one-dimensional profiles and is therefore more conservative.

Comparing the results obtained with different competing spatial templates, it is apparent

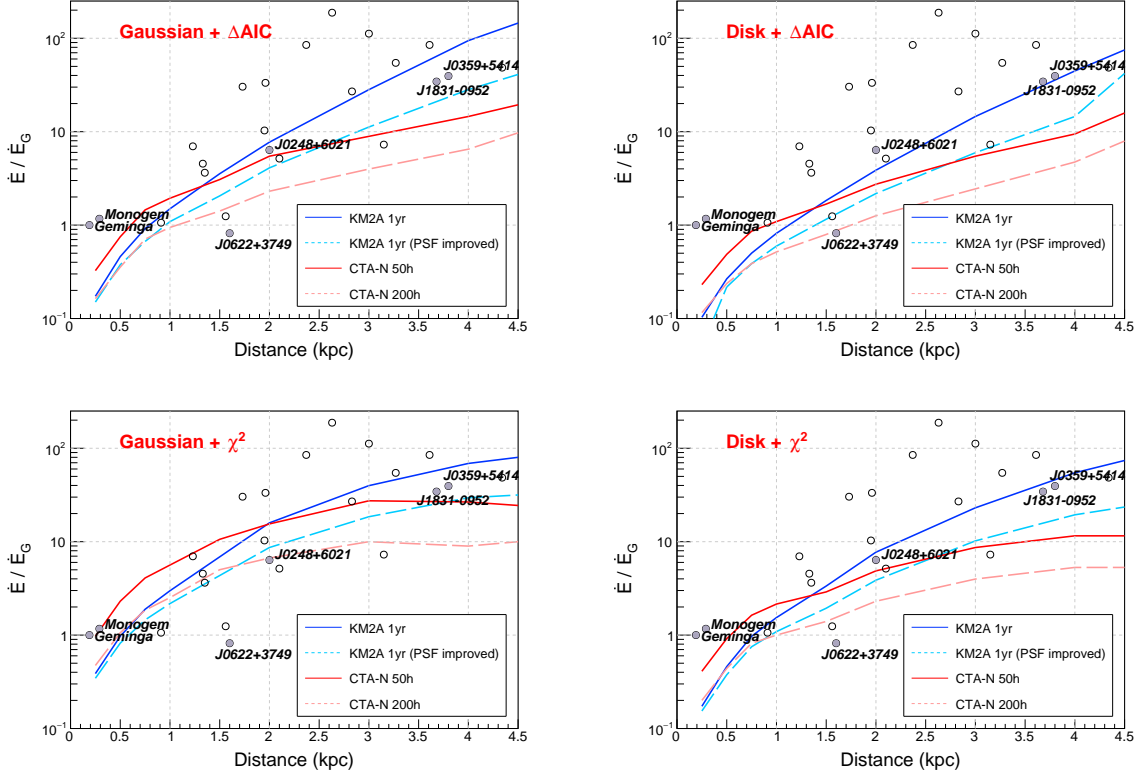


FIG. 2. Discrimination curves for pulsar halos achievable with CTA-North and LHAASO-KM2A. We use  $\dot{E}/\dot{E}_G$  instead of  $\dot{E}$  as the vertical axis, where  $\dot{E}_G$  denotes the luminosity of the reference source, Geminga. Sources located above the curves can be morphologically distinguished as diffusion halos. Filled circles denote known pulsar halos or candidates, while empty ones denote other pulsar-associated sources in the LHAASO catalog. The competing spatial models and statistical decision methods used in the four panels, from top left to bottom right, are as follows: Gaussian model with AIC, disk model with AIC, Gaussian model with  $\chi^2$  test, and disk model with  $\chi^2$  test.

that distinguishing diffusion templates from disk shapes is easier compared to differentiating them from Gaussian ones. This reflects the fact that disk models, characterized by flat central areas and sharp boundaries, differ more significantly from the smooth radial profiles produced by diffusion. On the other hand, Gaussian templates may partially mimic the central-peaked signature of diffusion halos, especially under conditions of restricted angular resolution or photon statistics.

The complementary performance of CTA and LHAASO-KM2A as a function of pulsar distance is clearly demonstrated. For relatively nearby objects ( $d \lesssim 1.5$  kpc), where the in-

intrinsic angular extension is large, both experiments are in principle capable of resolving the morphology. In this regime, the discrimination power is mainly driven by photon statistics rather than angular resolution. Owing to its nearly continuous operation, LHAASO-KM2A accumulates substantially higher event statistics, resulting in a stronger discrimination capability than CTA for relatively nearby halos. For more distant pulsar halos, the apparent angular size becomes smaller, and the discrimination power is increasingly limited by the PSF. In this regime, CTA outperforms LHAASO-KM2A despite its shorter exposure time, owing to its superior angular resolution. Although LHAASO-KM2A benefits from larger photon statistics, its broader PSF limits its ability to resolve subtle morphological differences at large distances.

The impact of enhanced instrumental performance is also clearly demonstrated. Improving the angular resolution of LHAASO-KM2A yields only marginal gains for nearby sources, as their morphology is already well resolved and the available photon statistics remain unchanged. In contrast, at larger distances, the improved PSF substantially extends the parameter space within which halos can be discerned, enabling the detection of sources that would otherwise remain unresolved. Increasing the CTA exposure time from 50 h to 200 h systematically enhances discrimination capability across both nearby and distant sources, since its angular resolution is already sufficient and the additional exposure primarily boosts the photon statistics.

Consistent with current observational results, LHAASO-KM2A can presently perform unambiguous morphological discrimination only for the nearby Geminga and Monogem halos. However, with a 40% improvement in angular resolution, LHAASO-KM2A would be able to identify several major pulsar halo candidates, namely the  $\gamma$ -ray halos surrounding pulsars J1831-0952, J0248+6021, and J0359+5414. With its nominal design performance and a typical exposure of 50 h, CTA is already capable of distinguishing the morphology of most candidate pulsar halos. The most challenging among the current candidates is the halo associated with LHAASO J0621+3755, as its pulsar has a spin-down luminosity comparable to that of Geminga but lies at a distance about six times larger. With an increased exposure of 200 h, CTA is expected to achieve morphological discrimination between the diffusion and disk templates for LHAASO J0621+3755. However, distinguishing the diffusion template from a Gaussian model would require even greater photon statistics.

## VI. CONCLUSION

We have investigated the capability of CTA and LHAASO-KM2A to identify pulsar halo candidates through morphological discrimination. Using realistic mock observations derived from diffusion-driven halo templates and instrument response functions, we compared the diffusion morphology against alternative, non-nested spatial templates, including Gaussian and disk models, employing both the AIC and the  $\chi^2$  test for statistical decision. The AIC criterion generally provides more optimistic results than the  $\chi^2$  test, allowing a larger fraction of halos to be distinguished from simplified morphologies. Diffusion halos are more easily separated from disk templates than from Gaussian ones, reflecting the stronger morphological contrast.

A clear complementarity between CTA and LHAASO-KM2A is presented. For relatively nearby halos with large angular extensions, LHAASO-KM2A benefits from higher photon statistics enabled by its large effective area and continuous operation. For more distant halos with smaller apparent sizes, CTA achieves superior discrimination owing to its much better angular resolution. In addition, improving angular resolution can significantly enhance the ability to identify distant pulsar halos for LHAASO-KM2A, such as LHAASO J0249+6022, HESS J1831–098, and the candidate halo around PSR J0359+5414. For CTA, by adopting longer observation times, it could in principle resolve the diffusion signatures of all candidate pulsar halos within 5 kpc, including LHAASO J0621+3755.

The discussion in this work is based on the ideal scenario where the object is an isolated source. If the target is contaminated by other nearby  $\gamma$ -ray sources, morphological discrimination could be more challenging. Furthermore, identifying diffusion signatures is a necessary but insufficient condition for confirming a pulsar halo; in practice, multi-wavelength observations are also required to determine whether a pulsar halo provides the most plausible interpretation.

## ACKNOWLEDGMENTS

This work is supported by the National Key R&D program of China under Grant No. 2024YFA1611401, and the National Natural Science Foundation of China under Grants No.

- [1] A. A. Abdo *et al.*, *Astrophys. J. Lett.* **664**, L91 (2007), arXiv:0705.0707 [astro-ph].
- [2] P. A. Caraveo, G. F. Bignami, A. De Luca, S. Mereghetti, A. Pellizzoni, R. Mignani, A. Tur, and W. Becker, *Science* **301**, 1345 (2003).
- [3] B. Posselt, G. Pavlov, P. Slane, R. Romani, N. Bucciantini, A. Bykov, O. Kargaltsev, M. Weiskopf, and C. Y. Ng, *Astrophys. J.* **835**, 66 (2017), arXiv:1611.03496 [astro-ph.HE].
- [4] A. U. Abeysekara *et al.* (HAWC), *Science* **358**, 911 (2017), arXiv:1711.06223 [astro-ph.HE].
- [5] K. Fang, *Front. Astron. Space Sci.* **9**, 1022100 (2022), arXiv:2209.13294 [astro-ph.HE].
- [6] R.-Y. Liu, *Int. J. Mod. Phys. A* **37**, 2230011 (2022), arXiv:2207.04011 [astro-ph.HE].
- [7] R. López-Coto, E. de Oña Wilhelmi, F. Aharonian, E. Amato, and J. Hinton, *Nature Astron.* **6**, 199 (2022), arXiv:2202.06899 [astro-ph.HE].
- [8] E. Amato and S. Recchia, *Riv. Nuovo Cim.* **47**, 399 (2024), arXiv:2409.00659 [astro-ph.HE].
- [9] A. Albert *et al.* (HAWC), *Astrophys. J.* **905**, 76 (2020), arXiv:2007.08582 [astro-ph.HE].
- [10] Z. Cao *et al.* (LHAASO), *Astrophys. J. Suppl.* **271**, 25 (2024), arXiv:2305.17030 [astro-ph.HE].
- [11] F. Aharonian *et al.* (LHAASO), *Phys. Rev. Lett.* **126**, 241103 (2021), arXiv:2106.09396 [astro-ph.HE].
- [12] M. Actis *et al.* (CTA Consortium), *Exper. Astron.* **32**, 193 (2011), arXiv:1008.3703 [astro-ph.IM].
- [13] G. Schwefer, R. Parsons, and J. Hinton, *Astropart. Phys.* **163**, 103008 (2024), arXiv:2406.17502 [astro-ph.HE].
- [14] B. M. Gaensler and P. O. Slane, *Ann. Rev. Astron. Astrophys.* **44**, 17 (2006), arXiv:astro-ph/0601081.
- [15] A. Albert *et al.* (HAWC), *Astrophys. J.* **974**, 246 (2024).
- [16] B. S. Acharya *et al.* (CTA Consortium), *Science with the Cherenkov Telescope Array* (WSP, 2018) arXiv:1709.07997 [astro-ph.IM].
- [17] C. T. A. Observatory and C. T. A. Consortium, “Ctao instrument response functions - prod5 version v0.1,” (2021).
- [18] S. Celli and G. Peron, *Astron. Astrophys.* **689**, A258 (2024), arXiv:2403.03731 [astro-ph.HE].
- [19] X. Bai, B. Y. Bi, X. J. Bi, Z. Cao, S. Z. Chen, Y. Chen, A. Chiavassa, X. H. Cui, Z. G.

- Dai, D. della Volpe, T. Di Girolamo, G. Di Sciascio, Y. Z. Fan, J. Giacalone, Y. Q. Guo, H. H. He, T. L. He, M. Heller, D. Huang, Y. F. Huang, H. Jia, L. T. Ksenofontov, D. Leahy, F. Li, Z. Li, E. W. Liang, P. Lipari, R. Y. Liu, Y. Liu, S. Liu, X. Ma, O. Martineau-Huynh, D. Martraire, T. Montaruli, D. Ruffolo, Y. V. Stenkin, H. Q. Su, T. Tam, Q. W. Tang, W. W. Tian, P. Vallania, S. Vernetto, C. Vigorito, J. . C. Wang, L. Z. Wang, X. Wang, X. Y. Wang, X. J. Wang, Z. X. Wang, D. M. Wei, J. J. Wei, D. Wu, H. R. Wu, X. F. Wu, D. H. Yan, A. Y. Yang, R. Z. Yang, Z. G. Yao, L. Q. Yin, Q. Yuan, B. Zhang, B. Zhang, L. Zhang, M. F. Zhang, S. S. Zhang, X. Zhang, Y. Zhao, X. X. Zhou, F. R. Zhu, and H. Zhu, (2019), arXiv:1905.02773.
- [20] Z. Cao *et al.* (LHAASO), *Chin. Phys. C* **48**, 065001 (2024), arXiv:2401.01038 [astro-ph.IM].
- [21] T. K. Gaisser, T. Stanev, and S. Tilav, *Front. Phys. (Beijing)* **8**, 748 (2013), arXiv:1303.3565 [astro-ph.HE].
- [22] F. Aharonian *et al.* (LHAASO), *Phys. Rev. Lett.* **126**, 241103 (2021), arXiv:2106.09396 [astro-ph.HE].
- [23] Z. Cao *et al.* (LHAASO), *Sci. China Phys. Mech. Astron.* **68**, 279504 (2025), arXiv:2410.04425 [astro-ph.HE].
- [24] K. Fang, S.-Q. Xi, L.-Z. Bao, X.-J. Bi, and E.-S. Chen, *Phys. Rev. D* **106**, 123017 (2022), arXiv:2207.13533 [astro-ph.HE].
- [25] K. Sabri, Y. Gallant, J. Devin, and K. Feijen, arXiv e-prints , arXiv:2510.03183 (2025), arXiv:2510.03183 [astro-ph.HE].
- [26] A. Albert *et al.* (HAWC), *Astrophys. J. Lett.* **944**, L29 (2023), arXiv:2301.04646 [astro-ph.HE].
- [27] T. Wach and A. M. W. Mitchell, arXiv e-prints , arXiv:2510.02802 (2025), arXiv:2510.02802 [astro-ph.HE].
- [28] A. De Sarkar, arXiv e-prints , arXiv:2601.21689 (2026), arXiv:2601.21689 [astro-ph.HE].